# Prediction of fluid occupancy in fractures using network modeling and x-ray microtomography. I: Data conditioning and model description

Zuleima T. Karpyn
*Department of Energy and Mineral Engineering, The Pennsylvania State University, University Park, Pennsylvania 16802-5000, USA*

Mohammad Piri*
*Department of Chemical and Petroleum Engineering, University of Wyoming, Laramie, Wyoming 82071-2000, USA*
(Received 25 November 2006; published 31 July 2007)

This paper presents a two-dimensional pore-scale network model of a rough-walled fracture whose inner structure had been mapped using x-ray microtomography. The model consists of a rectangular lattice of conceptual pores and throats representing local aperture variations. It is a two-phase model that takes into account capillary, viscous, and gravity forces. Mapping of fluids and fracture topology was done at a voxel resolution of $0.027 \times 0.027 \times 0.032$ mm$^3$, which allowed the construction of realistic fracture representations for modeling purposes. This paper describes the necessary data conditioning for network modeling, a different approach to determine advancing and receding contact angles from direct x-ray microtomography scans, and the network model formulation and methods used in the determination of saturation, absolute and relative permeabilities, capillary pressures, and fluid distributions. Direct comparison of modeled results and experimental observations, for both drainage and imbibition processes, is presented in the companion paper [M. Piri and Z. T. Karpyn, following paper, Phys. Rev. E 76, 016316 (2007)].

DOI: 10.1103/PhysRevE.76.016315 PACS number(s): 47.56.+r, 47.80.Jk, 91.60.Ba

## I. INTRODUCTION

Mapping the distribution of fluids in underground formations is of great importance for fields such as environmental remediation, geohazard mitigation, hydrology, geothermal exploitation, and hydrocarbon recovery. The ability to predict where fluids will migrate, and the characterization of fundamental transport properties, has motivated extensive research regarding multiphase flow through geologic formations. Many formations also present structural discontinuities that have great impact on the mobilization of fluids. Fractures are the most common form of discontinuity found in these systems. Fractures control the overall conductivity of the rock while the porous matrix provides fluid storage capacity. Understanding transport properties of fractures and their dependence on structure, fluids, and boundary conditions is essential for the design of effective recovery and remediation strategies.

Various approaches have been developed for the study of transport phenomena in fractures. They range from geometrical characterization of single fractures and fracture networks to transport processes, single and multiphase flow. Early work on computer-based network modeling dates back to the late 1950s [1–3]. In the past two decades, pore-scale network modeling has gained vast attention and has improved with the addition of features such as fluid trapping and wetting layers [4–9]. Dynamic network models allow the study of the effect of injection rate on residual saturations, relative permeabilities and the competition between various driving forces, i.e., capillary, viscous, and gravity forces, and their effects on displacement mechanisms, i.e., snapoff, cluster growth, and frontal advance [10–14]. Wetted structures and gravity fingers have been observed in network simulations of spontaneous imbibition in porous media including the effect of gravity [15]. Glass *et al.* [16] studied quasistatic immiscible displacement in horizontal, rough-walled fractures using modified invasion percolation models. They ignored viscous and gravity forces and also assumed that influence of local convergence (or divergence) of the fracture walls was ignorable. They examined the influence of the combined effect of two principle radii of curvature, in-plane and aperture-induced. This allowed the authors to model the experimentally reported saturation fronts. The dependence of capillary pressure and relative permeability characteristics on contact angles and void structures has also been investigated using pore-scale network models [17–20].

Proper characterization of the pore structure is crucial for the accuracy of multiphase displacement mechanisms implemented in pore network models. Experiments using statistical approaches, transparent epoxy replicas, and imaging techniques, e.g., nuclear magnetic resonance, serial section measurements of porous materials, and high resolution microtomography, have provided means to characterize aperture distributions and describe preferential flow paths in fractures [21–26]. In spite of recent advances in pore-scale representations of fractures and understanding of their flow characteristics, additional investigation is still needed. It is important to have a reliable physically-based tool able to predict macroscopic flow properties and fluid distributions in realistic fractures representation.

In this work, a highly detailed aperture distribution map constructed from x-ray microtomography scans is used to create a network of conceptual pores and throats representing the fracture's void structure. The fracture model presented in this study is a modified two-dimensional adaptation of a three-dimensional mixed-wet random pore-scale network model of two- and three-phase flow in porous media with

*mpiri@uwyo.edu

 

relative permeability predictions [27,28]. The approach is similar to the method utilized by Glass *et al.* [16], but the model has been extended to handle quasidynamic displacements taking into account rate and gravity effects. We also consider flow through wetting layers. The model recognizes three types of displacement: Pistonlike, cooperative pore filling ($I_n$ mechanisms [29]), and snapoff. The $I_n$ mechanisms allowed us to account for the effects of in-plane curvature; see Ref [16].

In the simulations presented in this paper, we compute pressures in both pores and throats, this is not the case, for instance, in the work by Hughes and Blunt [10]. Also we find threshold capillary pressures for displacements in pores and throats while Hughes and Blunt [10] allow the throats to be automatically filled after the neighboring pores are invaded. Various simulations were conducted to test the predictive capabilities of the model using a single fracture with highly detailed structure and fluid occupancy data. Paper I describes the conditioning of x-ray microtomography data and formulation of the two-dimensional, two-phase quasidynamic pore-scale network model. Paper II [30] presents modeling results for primary drainage, imbibition, and secondary drainage, as well as rigorous comparison of the predicted fluid occupancies with experimental results.

## II. EXPERIMENTAL OVERVIEW

### A. Core sample and imaging technique

Experimental results from previous work [31] are used in this study to construct a detailed two-dimensional conceptual network model of a rough fracture. In those experiments, a tensile fracture was induced on a cylindrical Berea sandstone core having 18% matrix porosity and 200 mD absolute permeability. The sample was 25.4 mm in diameter and 101.4 mm long. The two exposed fracture surfaces were ill-matched with a slight shift of 1 mm along the longitudinal axis to accentuate aperture changes inside the fracture. X-ray microtomography was used to determine fracture aperture variations, map the distribution of oil and water during drainage and imbibition, and determine contact angles. X-ray microtomography is a nondestructive imaging technique that uses x rays and mathematical reconstruction algorithms to view a cross-sectional slice of an object [32]. The image reconstruction is based on multiple x-ray measurements made through the object along different paths. The computed tomography (CT) system consists of an ionized x-ray source, a detector, a translation system, and a computer system that controls motions and data acquisition. The x-ray source has a Tungsten target with a focal spot of 5 microns. It produces a cone beam that passes through the core and activates the detector. The image intensifier detector surface releases electrons that are then focused on a screen that is photographed by a high-resolution ($1024 \times 1024$) camera with a frequency of 15 Hz. The sample is rotated 360° in the x-ray beam while the detector is providing attenuation views to the data acquisition computer. After the sample is rotated a complete turn, the system reconstructs a slice, which is a cross-sectional image of the attenuation values that represent a combination of the density and the apparent atomic number of the sample at the imaged position. The imager operates in volume mode where several separate slices are collected in one rotation. After each rotation, the sample is translated axially to a new scanning position, thus allowing a continuous three-dimensional coverage of the sample. The voxel resolution in the experimental data presented in this paper was $0.027344\ \text{mm} \times 0.027344\ \text{mm} \times 0.032548\ \text{mm}$, where 0.032548 mm indicates the slice thickness.

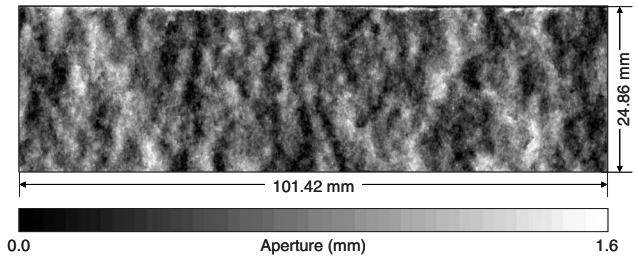


FIG. 1. Detailed fracture aperture map. Three-dimensional reconstruction of the scanned fractured sample allowed mapping of the fracture void and construction of a fracture aperture map. Dark and light gray represent small and large apertures, respectively.

### B. Fracture aperture characteristics

Three-dimensional reconstruction of the scanned fractured sample allowed mapping of the fracture void and construction of a detailed fracture aperture map. Figure 1 presents the aperture map obtained where dark and light gray represent small and large apertures, respectively. The scanned length was 101.42 mm and corresponds to the total sample length. The scanned diameter was 24.86 mm, 0.54 mm smaller than the actual core diameter (25.40 mm) to avoid core wall irregularities, maximize pixel resolution, and prevent direct exposure of x rays from the x-ray source to the detector. One should note that this was not done to exclude the high fracture apertures at the edges. The fracture aperture map presented in Fig. 1 provided the basis to construct the conceptual pore-scale network model representing the fracture. A fracture aperture histogram is presented in Fig. 2, indicating a maximum aperture of 1.60 mm and ap-

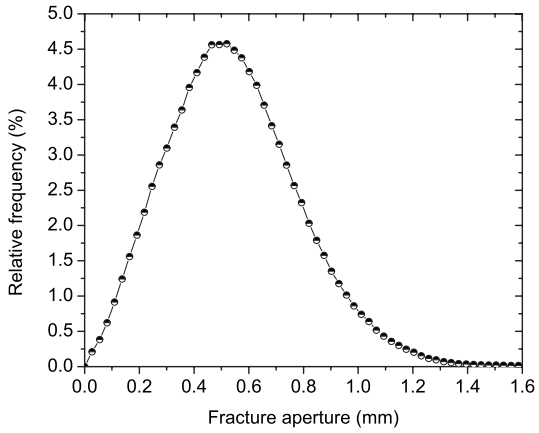


FIG. 2. Relative frequency distribution of fracture apertures.

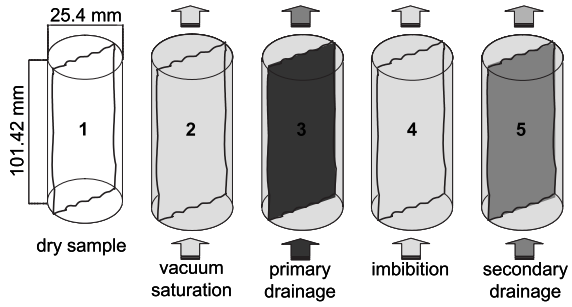


FIG. 3. Schematic of experimental stages performed in the fracture.

erture mode of 0.52 mm. The mean fracture aperture is 0.58 mm, and the standard deviation is 0.23 mm. Contact points in the fracture (zero aperture) sum 39.34 $mm^2$ and were excluded from the aperture histogram. The total contact area corresponds to 1.56% of the total rectangular area of the fracture, $101.42 \times 24.86$ $mm^2$.

### C. Core flooding

The experimental procedure consisted of monitoring fluid distribution inside a single rough fracture during several injection stages. These stages include primary drainage, or continuous oil injection into water; imbibition or continuous water injection into oil, and a simultaneous, one-to-one, injection of oil and water into the fracture. In the rest of this paper, parts I and II [30], we call this process secondary drainage due to the increase in oil saturation. Prior to primary drainage, the fractured sample (matrix and fracture) was vacuum-saturated with the water phase, which was a 15% by weight solution of sodium iodide, then scanned to confirm that no major air bubbles remained trapped inside the fracture. All these stages are schematically depicted in Fig. 3, and Table I presents a summary of the experimental flowing conditions and final oil saturation for each experimental stage. The matrix was fully saturated with the wetting phase (water) during all stages of the experiment. We think since the fracture was the preferential flow path for the nonwetting phase (oil) there was no significant exchange of nonwetting phase between the fracture and the matrix. This was confirmed by the x-ray images of the matrix at the end of all stages of the experiment. However, flow of water from the fracture into the matrix is quite possible and we had no means of preventing or monitoring it. As the wetting phase, water could flow into the matrix and bypass the fracture to reach the outlet, or return into the fracture at a different location, but we have no means of quantifying it experimentally. In the modeling part of this work we ignore this effect. But as an extension to this work, it would be interesting to model the fracture with permeable walls and look at its impact on fluid occupancy; see, for instance, Ref. [33]. The oil phase was a mixture of silicone oil and 30% by weight of *n*-decane. The aqueous phase was brine with 15% by weight NaI. We will use phrase "water" for the aqueous phase in the rest of the paper. Measured viscosities and densities at 25 °C were 5.0 cP and 0.89 $g/cm^3$ for the oil phase, and 1.2 cP and 1.11 $g/cm^3$ for the water phase. The interfacial tension of this oil-water system, 41.2 mN/m, was measured in the laboratory using the DuNouy ring method [34]. Precise representation of experimental conditions, fracture structure, fluid properties, and wetting characteristics were essential for the construction of the network model presented in this paper.

### D. Experimental data

Visualization of fluid occupancy inside the fracture during primary drainage, imbibition, and secondary drainage was possible using x-ray microtomography. Mechanisms such as fluid trapping, preferential flow paths, and coalescence and redistribution of liquid globules were observed. Findings from those laboratory experiments demonstrated strong correspondence between fluid distribution and the mismatch of the fracture surfaces [31]. Figure 4 shows the distribution of oil globules inside the fracture, relative to the dry aperture map on the left. The globules of oil in the two-dimensional maps are denoted in green, while the gray zones represent local fracture apertures filled with water. Oil globules match most areas in light gray on the aperture map, confirming the presence of water in the narrowest gaps (dark gray). Some oil globules in the imbibition map appear to be truncated by a horizontal line. These discontinuities resulted from the scanning process when, coincidentally, globules changed positions while being scanned, thus creating a fictitious globule discontinuity. The three occupancy maps shown in Fig. 4 were used in the present study as a comparative platform to

TABLE I. Summary of experimental flowing conditions and final saturations in the fracture.

| Experimental stage | Initial injection rate (cc/min) | Initial injection time (min) | Continued injection rate (cc/min) | Continued injection time (min) | Final $S_o$ | Final $S_w$ |
|---|---|---|---|---|---|---|
| Vacuum saturation: water into air | | | | | 0.0 | 1.0 |
| Primary dr.[a]: continuous oil inj.[b] | 0.5 | 12 | 0.05 | 300 | 0.65 | 0.35 |
| Imbibition: continuous water inj. | 0.5 | 12 | 0.05 | 300 | 0.37 | 0.63 |
| Secondary dr.: simultaneous inj. of oil and water | 0.25each | 150 | 0.1 each | 300 | 0.58 | 0.42 |

[a]Drainage.
[b]Injection.

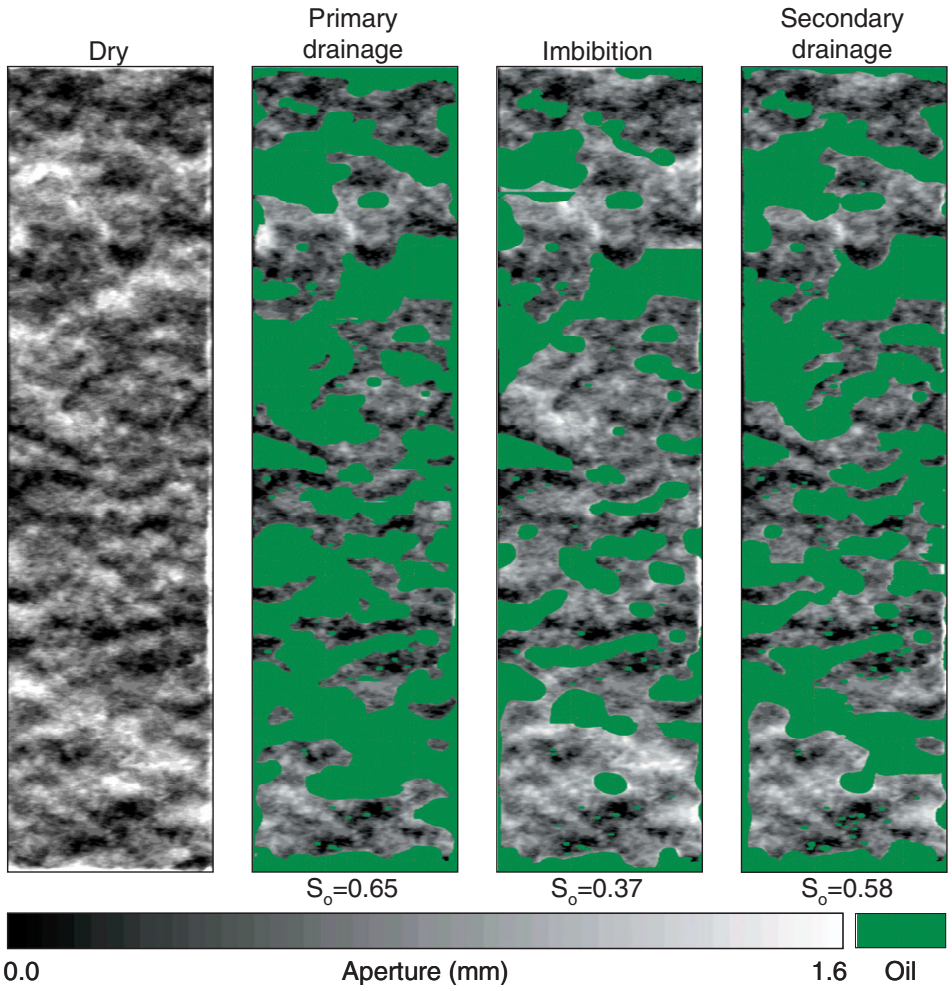


FIG. 4. (Color) Oil residence relative to local fracture aperture generated by x-ray microtomography at the end of different experimental stages [31].

test the accuracy of the equivalent pore-scale network model at the same final saturations; 65% oil saturation at the end of primary drainage, 37% during imbibition, and 58% during secondary drainage. The structure and location of the oil globules residing in the fracture are compared and discussed.

## III. DATA CONDITIONING FOR NETWORK MODELING

### A. Coarse fracture representations

The original fracture aperture map obtained from CT scans contains a total of 2 832 444 elements with variable apertures. An equivalent network model preserving such resolution would be extremely large and computationally expensive. Therefore, four coarser versions of the original high-resolution fracture aperture map (OHRM) were created. Table II presents a list of the geometric characteristics and statistical information for the networks that were constructed using four coarse maps (A through D) and the original map at the highest resolution. The tabulated information includes the number of elements, directional resolution, fracture width, length, volume, and contact area. The level of coarsening increases from map A to map D, as depicted in Fig. 5. The mathematical algorithm constructed to generate the coarse aperture maps imposes the preservation of total contact area. Initially, only nonzero apertures are averaged in the calculation of the equivalent coarse apertures. Groups containing zero-aperture points are ranked according to their proportion of zero-apertures in decreasing order. Finally, groups with the largest zero-aperture ratio are converted into solid contacts in the new coarse-resolution map. The conversion stops when the contact area in the new coarse-resolution map is the closest to the actual high-resolution contact area. Each of the four coarse aperture maps was generated from the original high-resolution map to build an equivalent network model. The effect of resolution on simulation results is discussed in the results and discussions section of this paper (part II).

### B. Determination of contact angles from x-ray microtomography

Contact angle is an important indicator of the wetting characteristics of a fluid-solid system. It is defined as the angle between the two-phase line and the solid surface mea-

TABLE II. Geometric characteristics and statistical information for the networks that were constructed from the original high-resolution aperture map and four coarser versions of it.

| Item | OHRM[a] | A | B | C | D |
|---|---|---|---|---|---|
| $N_l$[b] | 3116 | 779 | 389 | 283 | 222 |
| $N_w$[c] | 909 | 303 | 113 | 75 | 69 |
| $N_t$[d] | 2 832 444 | 236 037 | 43 957 | 21 225 | 15 318 |
| $N_{\text{inlet}}$[e] | 909 | 303 | 113 | 75 | 69 |
| $N_{\text{outlet}}$[f] | 909 | 303 | 113 | 75 | 69 |
| $N_P$[g] | 1 394 084 | 116 194 | 21 635 | 10 447 | 7533 |
| $N_T$[h] | 1 394 158 | 116 159 | 21 631 | 10 443 | 7542 |
| $\bar{a}$[i] (mm) | 0.5838 | 0.5852 | 0.5833 | 0.5817 | 0.5773 |
| $a_{\max}$ (mm) | 5.2227 | 4.949 264 | 4.293 | 4.183 632 | 4.128 944 |
| $a_{\min}$ (mm) | 0.027 344 | 0.027 344 | 0.054 688 | 0.082 032 | 0.082 032 |
| $CN_{\text{avg}}$[j] | 3.987 96 | 3.9672 | 3.9418 | 3.926 76 | 3.922 |
| $R_a$[k] (mm) | 0.027 344 | 0.027 344 | 0.027 344 | 0.027 344 | 0.027 344 |
| $R_w$ (mm) | 0.027 344 | 0.082 031 | 0.218 750 | 0.328 125 | 0.355 469 |
| $R_l$ (mm) | 0.032 548 | 0.130 192 | 0.260 384 | 0.358 028 | 0.455 672 |
| Width (mm) | 24.85 | 24.85 | 24.718 75 | 24.609 37 | 24.527 36 |
| Length (mm) | 101.42 | 101.4196 | 101.2894 | 101.3219 | 101.1592 |
| $N_{\text{asp}}$[l] | 44202 | 3684 | 691 | 335 | 243 |
| $V$[m] ($\text{mm}^3$) | 1471.65 | 1475.30 | 1460.43 | 1450.406 | 1432.51 |
| CA[n] ($\text{mm}^2$) | 39.3394 | 39.3443 | 39.3587 | 39.3551 | 39.3605 |

[a]Original high-resolution map.
[b]Number of elements along the length.
[c]$w$=width.
[d]Total number of elements.
[e]Number of elements connected to the inlet.
[f]Number of elements connected to the outlet.
[g]Number of pores.
[h]Number of throats.
[i]$a$=aperture; $\bar{a}$=average aperture.
[j]Average coordination number.
[k]Resolution in the aperture direction.
[l]asp=asperities.
[m]$V$=volume.
[n]CA=contact area due to asperities.

sured traditionally through the denser phase. Figure 6(a) shows a schematic diagram of a two-phase system on a horizontal solid surface, indicating the interfacial forces acting on the system and the corresponding contact angle. In a two-phase system, where oil and water reside on a solid, a horizontal force balance can be written as

$$\sigma_{os} - \sigma_{ws} = \sigma_{ow} \cos \theta_{ow}, \tag{1}$$

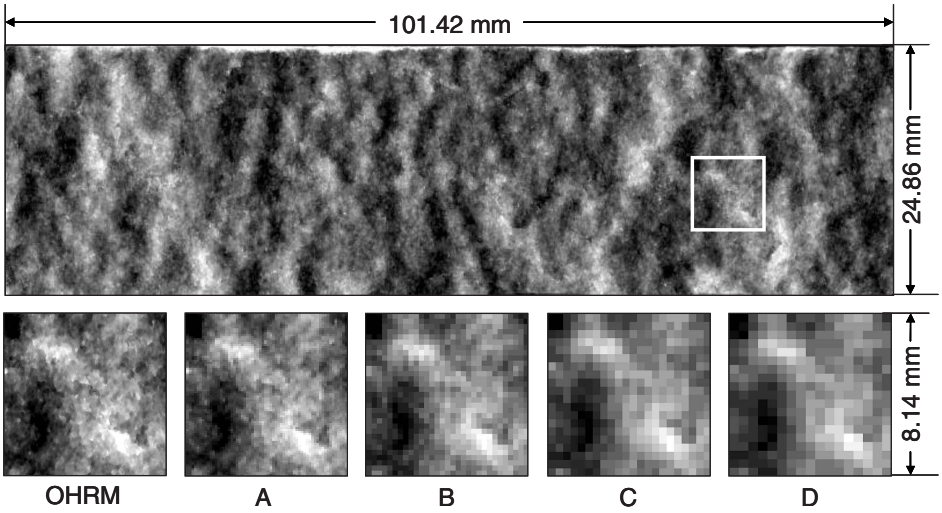


FIG. 5. Coarse fracture aperture representations relative to the original high resolution map (OHRM): 250×250 pixels, A: 83×62 pixels, B: 31×31 pixels, C: 20×22 pixels, and D: 19×17 pixels.

where $\theta_{ow}$ is the contact angle and $\sigma$ is an interfacial tension between two phases labeled $o$, $w$, or $s$ to represent oil, water, or solid, respectively.

The greater the adhesion of the denser phase to the solid, the smaller the contact angle. The contact angle in a fracture with nonparallel surfaces is presented in Fig. 6(b), where $r$ is the principal radius of curvature, $a$ is the fracture aperture at the triple interface, and $\beta$ is the fracture surface inclination. If we define a line of symmetry between the two fracture surfaces, $r$ is related geometrically to the local aperture, the fracture surface angle, and the contact angle through the following expression:

$$r = \frac{a}{2\cos(\beta + \theta_{ow})}. \quad (2)$$

The x-ray imaging technique described in this paper allowed a detailed mapping of fracture apertures and fracture topography, as well as the visualization of oil-water interfaces, from which contact angles can be estimated. Figure 7 shows a CT scan obtained during primary drainage (a), a magnification of the oil-water interface in the fracture (b), and the same magnified section in the dry sample (c). Oil and water coexist in the fracture at preferential locations. In general, water occupies narrow apertures while oil prefers large gaps. In order to provide an accurate representation of the fluid flow system under study, contact angles were estimated from the CT slices obtained during the core flooding experiment. Due to the difficulty of measuring radius of curvature directly from CT images, the authors implemented an inverse-solution approach to determine contact angle from x-ray microtomography scans. For a given fracture geometry, a trial contact angle is imposed. Then, radius of curvature and fluid occupancy are modeled using a wetting-phase growth model at constant contact angle. Results from this model are compared against CT data, and a close estimation

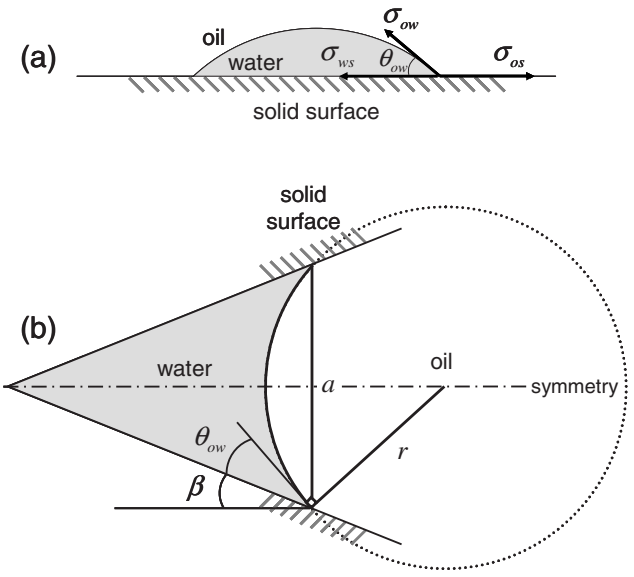


FIG. 6. Contact angle in oil-water-solid systems, (a) contact angle and interfacial force balance on a horizontal surface, and (b) radius of curvature and contact angle on diverging surfaces.

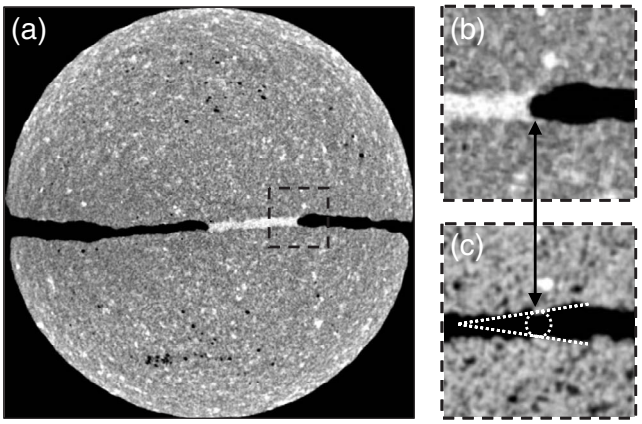


FIG. 7. Interfacial curvature during primary drainage, (a) CT slice obtained 22.88 mm above the bottom (inlet) of the core, (b) magnification of oil-water interface, and (c) magnification of fracture surface extracted from dry CT slice at the same location.

of contact angle is reached when the imposed angle gives an accurate representation of the fluid distribution and the interfaces observed experimentally.

Figure 8 shows the simulated interfacial curvature for a CT slice located 22.88 mm above the bottom of the core, at an imposed contact angle of 10°. The top image (a) is a cropped section of the original CT slice, and the images below [(b) through (e)] are intermediate results from the model developed for the determination of contact angles. Water growth is controlled by changes in radius of curvature using a constant contact angle. Water invasion stops when the final fluid saturation approaches that in the original CT slice. As water fills the fracture in the model, oil is assumed to migrate

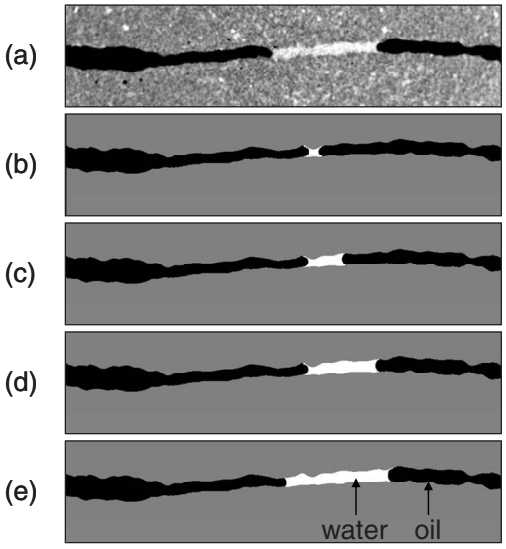


FIG. 8. Progression of simulated interfacial curvature 22.88 mm above the bottom (inlet) of the core for 10° contact angle. (a) Original CT section at $S_w$=0.179, (b) $S_w$=0.017, (c) $S_w$=0.061, (d) $S_w$=0.120, and (e) $S_w$=0.179. Note: (b) through (e) are intermediate results generated by the model developed for the determination of contact angles.

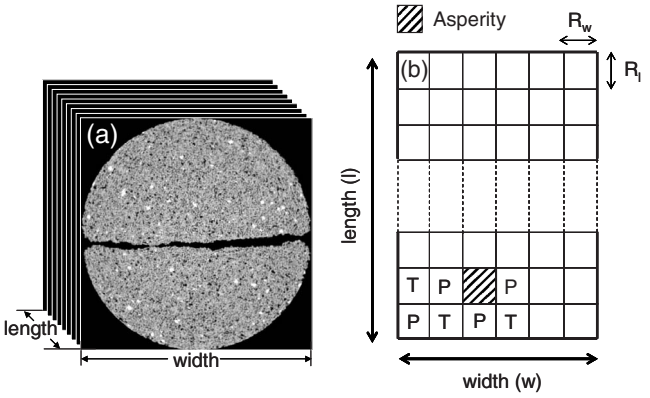


FIG. 9. Schematic representation of network construction, (a) CT slices of the fractured sample, and (b) regular lattice of conceptual pores (P) and throats (T) in the fracture.

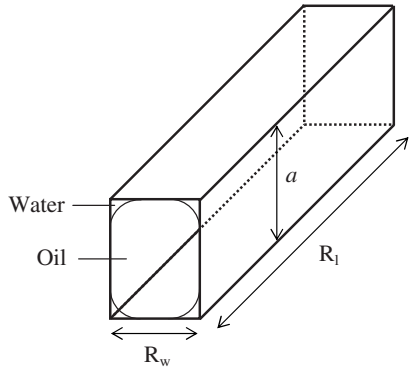


FIG. 10. A capillary tube with rectangular cross section.

in the direction perpendicular to the slice. Water appearance starts at the smallest fracture apertures in the fracture cross section. The image at the bottom of Fig. 8 demonstrates a satisfactory representation of fluid distributions compared to those obtained experimentally.

The magnitude of the contact angle depends on the direction of displacement. This difference between *advancing*, i.e., wetting phase displacing the nonwetting phase, and *receding*, i.e., nonwetting phase displacing the wetting phase, is called contact angle hysteresis and may be as large as 50°–90° [34–36] depending on surface roughness, surface heterogeneity, swelling, rearrangement, or alteration of the surface by solvent [34]. Four different contact angles at two different locations were examined, and results were compared against the experimental CT slices: 5, 10, 15, and 20° for receding contact angle and 20, 25, 30, and 35° for advancing contact angle. Receding and advancing contact angles for the system under study were found to be 10° and 25°, respectively. We assume there is no wettability alteration owing to contact between the oil phase and the solid surface of the fracture. In other words, the contact angle hysteresis in this work is only due to direction of displacement.

## IV. NETWORK MODEL

We present a two-dimensional network model of conceptual pores and throats in order to simulate two-phase flow in the tensile fracture described in Sec. II. In this section we show how the network was constructed, and describe the procedures used to compute threshold capillary pressures, saturations, pressure fields, and absolute and relative permeabilities.

### A. Description

A two-dimensional regular lattice of conceptual pores and throats, Fig. 9(b), is generated to present the variations in the aperture of the fracture (see Fig. 11). The model allows us to capture the complex topological features of the fracture's inner structure. Table II lists statistical information for each network used in this work.

The pore-scale network model employed in this work was originally developed by Piri and Blunt [27,28]. It is capable of reading as input any two- or three-dimensional regular or random network comprised of pores connected by throats. It has been successfully used to predict two- and three-phase relative permeabilities in Berea sandstone [28]. In this work, we extend the capabilities of the model by implementing rate and gravity effects. We then feed the two-dimensional networks that were constructed using the coarse aperture maps described in Sec. III A. The aperture maps and the resolutions along the width and length of the fracture were used to assign appropriate dimensions to each pore and throat. We consider each element as a pore or throat only because of a specific input format required by the network model, but pores and throats are treated exactly the same in all the modeling procedures we utilize. Therefore, local aperture size does not determine whether an element is a pore or a throat and a pore does not necessarily have an aperture greater than a neighboring throat. We start from the lower-left corner of the network assigning a "P" (for pore) or "T" (for throat) to each element with a known aperture using the pattern depicted in Fig. 9(b). Each pore is connected to throats (not pores) and vice versa. After skipping an asperity we make sure that this condition is still satisfied. Each pore or throat is connected to a maximum of four neighboring elements (see Table II for average coordination number for each network) and is rectangular in cross section with the local aperture, $a_k$, being the height, and the resolution along the width of the fracture, $R_w$, being the width of the element (see Fig. 10). Each pore or throat is also assigned a length, $R_l$, equal to the scanning resolution along the length of the fracture. Thus the total volume of each element becomes $V_k = a_k \times R_w \times R_l$. One should note that $a_k = n_k \times R_a$, where $n_k$ is the number of pixels for aperture in element $k$ and $R_a$ is the resolution in the aperture direction. The angular cross section shown in Fig. 10 allows the wetting phase to occupy the corners when the nonwetting phase fills the center.

The displacement mechanisms incorporated in the model are based on the physics of multiphase flow observed in micromodel experiments. The model calculates threshold capillary pressures for three different displacement mechanisms that are relevant to the processes that we simulate, i.e., pis-

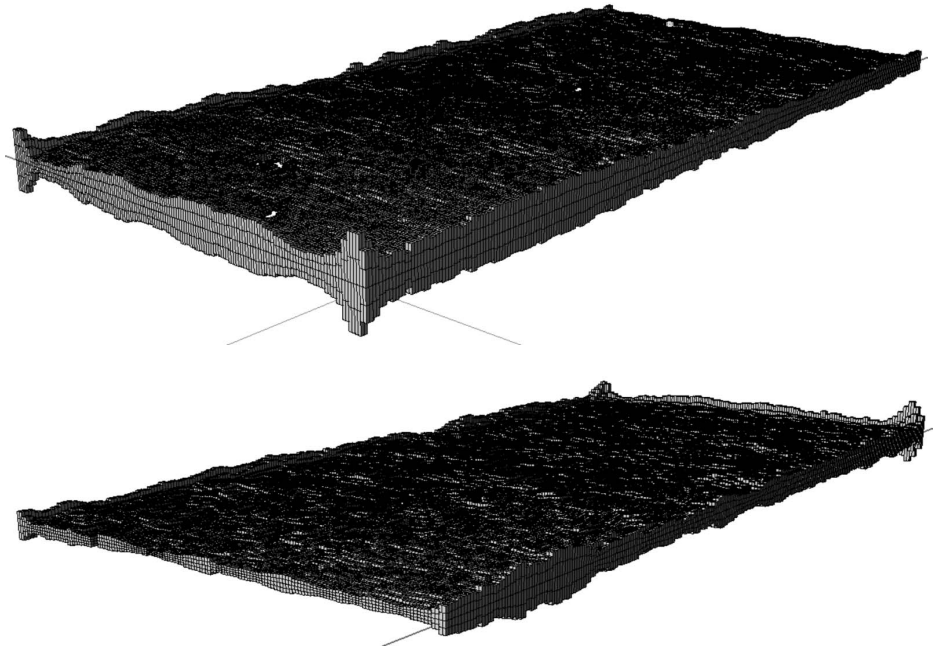

FIG. 11. Three-dimensional visualization of the fracture topology using coarse aperture map C (see Table II). One should note that the network was visualized assuming, for illustrative purposes, that the reference plane is located at the center resulting in a symmetric three-dimensional image.

tonlike displacement, snapoff, and cooperative pore filling. A series of pore-level displacements are combined in order to simulate different two-phase processes. For each process, the model uses pertinent displacement mechanisms. It also takes into account contact angle hysteresis in the computation of threshold capillary pressures.

To find the pressure difference across an interface we use the Young-Laplace equation:

$$P_i - P_j = \sigma_{ij}\left(\frac{1}{r_1} + \frac{1}{r_2}\right), \tag{3}$$

where $r_1$ and $r_2$ are the principal radii of curvature, and $P_i$ and $P_j$ are pressures of the phases on either side of the interface. There are two types of interface under such conditions: *(I) Main terminal meniscus (MTM)* [37], which is the invading meniscus at the pore-throat junction separating wetting and nonwetting fluids. The shape of such meniscus in a cylindrical tube of uniform wetting is spherical meaning that the two radii of curvature are the same ($r_1 = r_2 = r$). The pressure difference across an MTM is then given by

$$P_i - P_j = \frac{2\sigma_{ij}}{r}. \tag{4}$$

*(II) Arc meniscus (AM)*, which is the interface at a corner of a noncircular element (see Fig. 10). It is assumed that the curvature of the interface is negligible parallel to an element meaning that the principal radii of curvature would be $r_1 = r$ and $r_2 = \infty$ [34,37]. The pressure difference across such an interface is given by

$$P_i - P_j = \frac{\sigma_{ij}}{r}. \tag{5}$$

Pistonlike displacement refers to the displacement of one phase in the center of an element by another residing in the center of a neighboring element. In other words, once the threshold capillary pressure is reached, the MTM that has access to the entrance of the element moves into the capillary with a fixed curvature filling the center of the element with the invading phase. While the MTM displaces the defending phase from the center of the element, the residual of the displaced phase—in *noncircular* elements—may remain in the corners creating *new* AMs (see Fig. 10). This happens only if

$$\theta_{ij} < \frac{\pi}{2} - \alpha, \tag{6}$$

where $\theta_{ij}$ is the angle that the new AMs make with the solid surface towards the apex of the corner, which is the contact angle in this case, and $\alpha$ is the corner half angle. If the effect of gravity is ignored then the curvature of the AMs will be exactly the same as that of the invading MTM [37].

Every displacement is either drainage or imbibition. Drainage in a capillary element is referred to an event where a wetting phase is displaced by a nonwetting phase, while an event in which a nonwetting phase is displaced by a wetting phase is called imbibition. Pistonlike displacement can take place in both cases.

The prevailing contact angles during pistonlike drainage and imbibition events are receding and advancing values, respectively. In the absence of contact angle hysteresis, the

threshold capillary pressure of pistonlike imbibition is the same as that of drainage, otherwise during imbibition, when the relevant capillary pressure is reduced, each interface starts hinging from the receding contact angle towards the advancing value. Interface in each corner stays pinned as long as the hinging value is smaller than the advancing contact angle. The wetting phase will enter the element when the advancing contact angle is reached. The threshold capillary pressures are found using the Mayer-Stowe-Princen (MS-P) method described in Sec. IV B.

To accommodate drainage and imbibition displacement processes, we assign two contact angles to each pore and throat: $\theta^r_{ow}$ receding contact angle for oil displacing water (drainage) and $\theta^a_{ow}$ advancing contact angle for water displacing oil (imbibition).

### B. Threshold capillary pressures

The threshold capillary pressures for pistonlike displacements are calculated using the Mayer-Stowe-Princen (MS-P) method [38–41]. The MS-P method is based on equating the pressure difference across the AMs, given by Eq. (5) for elements with straight walls, left at the corners of the capillary tube by the pistonlike displacement, to that of the MTM which is found from an energy balance for MTM invasion.

Consider a capillary element with rectangular cross section filled with a defending phase in the center and an invading phase having access at one end, forming an MTM. An increase in the pressure of the invading phase to the threshold value, when the pressure of the defending phase is fixed, results in the MTM entering the capillary with a fixed curvature and changing fluid configurations (old to new) at the corners. Assuming that the system is closed, at equilibrium, the MTM spherical, the solid a rigid phase ($dV_s=0$), and the solid walls straight, for a small movement, $dx$, of an MTM in the capillary where two fluids, oil ($o$) and water ($w$), may be present, the Helmholtz free energy balance can be written as [42]

$$dF = -\sum_{i=o,w} P_i dV_i + \sum_{ij=\mathrm{ow,os,ws}} \sigma_{ij} dA_{ij}, \tag{7}$$

where $P$ is the pressure, $V$ is the volume, $\sigma_{ij}$ is the interfacial tension, and $A_{ij}$ is the fluid-fluid or fluid-solid contact area. Also

$$dV_i = \{[A_{i,t}]^{\mathrm{nc}} - [A_{i,t}]^{\mathrm{oc}}\}dx, \tag{8}$$

$$dA_{ij} = \{[L_{ij,t}]^{\mathrm{nc}} - [L_{ij,t}]^{\mathrm{oc}}\}dx, \tag{9}$$

where superscripts nc and oc stand for new and old fluid configurations, respectively, $A_{i,t}$ is the total area occupied by phase $i$ in the cross section, and $L_{ij,t}$ is the total length of contact between phases $i$ and $j$ in the cross section.

A system with constant temperature and constant total volume is at equilibrium when the Helmholtz free energy $F$ is minimum [43] or

$$dF = 0. \tag{10}$$

The total area of the cross section, $(A_t)_k$, and perimeter, $(L_t)_k$, of capillary $k$ with rectangular cross section are given by

$$(A_t)_k = a_k \times R_w = [A_{o,t}]^{\mathrm{nc}} + [A_{w,t}]^{\mathrm{nc}} = [A_{o,t}]^{\mathrm{oc}} + [A_{w,t}]^{\mathrm{oc}}, \tag{11}$$

$$(L_t)_k = 2 \times (R_w + a_k) = [L_{os,t}]^{\mathrm{nc}} + [L_{ws,t}]^{\mathrm{nc}} = [L_{os,t}]^{\mathrm{oc}} + [L_{ws,t}]^{\mathrm{oc}}. \tag{12}$$

For drainage pistonlike displacement $[A_{o,t}]^{\mathrm{oc}}=0$, $[L_{os,t}]^{\mathrm{oc}}=0$ and $[L_{ow,t}]^{\mathrm{oc}}=0$ as we inject oil into elements fully saturated with water. And for imbibition pistonlike displacement $[A_{o,t}]^{\mathrm{nc}}=0$, $[L_{\mathrm{os},t}]^{\mathrm{nc}}=0$ and $[L_{\mathrm{ow},t}]^{\mathrm{nc}}=0$ since water invasion into a water-wet angular capillary tube with oil in the center and water in the corners leads to a fully saturated fluid configuration. Therefore, from Eqs. (1), (5), and (7)–(12) the threshold capillary pressure for drainage is derived as

$$P^{\mathrm{th}}_{\mathrm{cow}} = \frac{\sigma_{\mathrm{ow}}}{r_{\mathrm{ow}}} = \frac{\sigma_{\mathrm{ow}}[L_{\mathrm{ow},t} + L_{\mathrm{os},t}\cos\theta^r_{\mathrm{ow}}]^{\mathrm{nc}}}{[A_{o,t}]^{\mathrm{nc}}}, \tag{13}$$

where $L_{\mathrm{ow},t}=4L_{\mathrm{ow},c}$, $L_{\mathrm{os},t}=L_t-8b$, and $[A_{o,t}]^{\mathrm{nc}}=A_t-4A_{w,c}$. $L_{\mathrm{ow},c}$, $b$, and $A_{w,c}$ are the length of contact line between oil and water, meniscus-apex distance of the interface, and the area occupied by water at a corner, respectively. These are calculated using Eqs. (A1)–(A3) with $\theta_k=\theta^r_{\mathrm{ow}}$ and $r_{\mathrm{ow}}=r^d_{\mathrm{ow}}=\sigma_{\mathrm{ow}}/P^d_{\mathrm{cow}}$ (see Appendix A), where superscript $d$ stands for drainage. For an imbibition pistonlike displacement one may use Eq. (13) with $\theta^r_{\mathrm{ow}}$ replaced by $\theta^a_{\mathrm{ow}}$ to calculate the threshold capillary pressure. Also $L_{\mathrm{ow},c}$ and $A_{w,c}$ are computed using Eqs. (A1) and (A3), respectively, with $\theta_k=\theta^h_{\mathrm{ow}}$ and $r_{\mathrm{ow}}=r^{\mathrm{im}}_{\mathrm{ow}}=\sigma_{\mathrm{ow}}/P^{\mathrm{im}}_{\mathrm{cow}}$, where superscript im stands for imbibition. $\theta^h_{\mathrm{ow}}$ is used only when it is less than $\theta^a_{\mathrm{ow}}$; otherwise, $\theta^a_{\mathrm{ow}}$ is used. To calculate $b$ we use Eq. (A2) with $\theta_k=\theta^r_{\mathrm{ow}}$ and $r_{\mathrm{ow}}=r^d_{\mathrm{ow}}$ for $\theta^h_{\mathrm{ow}}\le\theta^a_{\mathrm{ow}}$ and with $\theta_k=\theta^a_{\mathrm{ow}}$ and $r_{\mathrm{ow}}=r^{\mathrm{im}}_{\mathrm{ow}}$ for $\theta^h_{\mathrm{ow}}>\theta^a_{\mathrm{ow}}$. $\theta^h_{\mathrm{ow}}$ is found using Eq. (A4) (see Appendix A).

During imbibition, displacement of oil from the center of each element may also be carried out by a cooperative pore filling mechanism where threshold capillary pressure depends on aperture of the element and the number of neighboring elements that do not hold the invading phase in the center. For an element with coordination number $m$, $m-1$ cooperative pore filling events are possible, called $I_n$, where $n$ is the number of neighboring element that are not involved in the displacement, $1\le n\le m-1$ [29,44]. When $n=1$, the displacement is a pistonlike event and the threshold capillary pressure is given by Eq. (13). But for $I_3$ and $I_2$ displacement events, we use [10,29]

$$P^{\mathrm{th}}_{\mathrm{cow}} = \frac{2\sigma_{\mathrm{ow}}\cos\theta^a_{\mathrm{ow}}}{a_k}, \tag{14}$$

$$P^{\mathrm{th}}_{\mathrm{cow}} = \sigma_{\mathrm{ow}}\left\{\frac{2\cos\theta^a_{\mathrm{ow}}}{a_k} + \frac{1}{R_w} - \frac{1}{\sqrt{2}R_w}\right\}. \tag{15}$$

Snapoff corresponds to an event where oil in the center of an element is displaced by water residing in corners. When oil-water capillary pressure decreases, the invading phase

TABLE III. Absolute permeability of the maps A to D listed in Table II.

| Item | $K(m^2)$ |
|---|---|
| A | $2.556\times10^{-10}$ |
| B | $1.035\times10^{-9}$ |
| C | $1.665\times10^{-9}$ |
| D | $1.881\times10^{-9}$ |

starts swelling and consequently contributing AMs may hinge and eventually move—when the hinging contact angle reaches the advancing value—towards the center to meet the other moving AMs. When AMs meet, the center of the element is filled spontaneously by the displacing phase. Snapoff is not favored over a pistonlike or cooperative pore filling event when there is a neighboring element with the invading phase in the center that is able to carry out the displacement. The threshold capillary is calculated using

$$P_{\mathrm{cow}}^{\mathrm{th}} = \frac{2\sigma_{\mathrm{ow}}(\cos\theta_{\mathrm{ow}}^{a} - \sin\theta_{\mathrm{ow}}^{a})}{a_k}. \tag{16}$$

We assume snapoff takes place when meniscus-apex distance of oil-water interface in a corner of element $k$ becomes equal to $a_k/2$.

## V. SATURATION, CONDUCTANCE, AND PRESSURE FIELD CALCULATIONS

Saturation and relative permeability in a capillary dominated process are only computed when invading phase pressure reaches a new maximum—this means that the system is at equilibrium and it is not possible to carry out any displacements with the current phase pressures. The capillary pressure is found from the pressure difference between continuous phases. If $V_p^k$ is the volume of phase $p$ in element $k$ then the saturation of phase $p$ in the system is given by

$$S_p = \frac{\sum_{k=1}^{n_e} V_p^k}{\sum_{k=1}^{n_e} (V_w^k + V_o^k)}, \tag{17}$$

where $n_e$ is the total number of elements. Volume of a phase in an element is the total volume of that element multiplied by the fraction of the cross-sectional area occupied by that phase.

When saturation is computed, relative permeability and capillary pressure can also be found. This is not done after every saturation computation to save computer time. To compute absolute and relative permeability, conductance of each continuous phase location in each element is computed first. Normally exact analytic results are not possible, and semiempirical expressions derived from solutions of the Stoke's equation for flow in pores of different geometries, and for different fluid configurations, are used [45–51]. Then the average conductance for each continuous phase in the network is computed, by explicitly calculating the flow through the network assuming conservation of volume. From this absolute and relative permeability can be found [48,50,52,53].

In order to minimize the influence of end effects on the calculated macroscopic properties, we calculate saturation within two surfaces perpendicular to the main flow direction bounding the central 90% of the network. However, pressures are solved over the entire network for each pore and throat. Then, the average pressure of the fluid whose permeability is being calculated is found at the two surfaces located, for instance, at $0.05L$ and $0.95L$ from the inlet, where $L$ is the total length of the fracture. The absolute permeability of the network is calculated using Darcy's law:

$$K = \frac{\mu^{\varrho} Q_{\mathrm{total}}^{\varrho} L}{A\Delta P}, \tag{18}$$

where $K$ is the absolute permeability, $\mu^{\varrho}$ is the viscosity of fluid $\varrho$, $L$ is the distance between the aforementioned surfaces, and $\Delta P$ is the corresponding pressure drop. $A$ is the cross-sectional area perpendicular to the main direction of flow and $Q_{\mathrm{total}}^{\varrho}$ is the total flow rate of fluid $\varrho$.

The network is assumed to be completely saturated with only one phase, $\varrho$, initially and conductivity of each fully saturated element is calculated from [48,54,55]

$$g^{\varrho} = \frac{\pi r_h^4}{8\mu^{\varrho}}, \tag{19}$$

where $r_h$ is the hydraulic radius that is given by [10]

$$r_h = 0.5 \times \left\{ \sqrt{\frac{A_t}{\pi}} + \frac{a}{2} \right\}, \tag{20}$$

where $A_t$ is the total cross-sectional area of the element. When a network has elements with noncircular cross section, a single element might accommodate more than one fluid in it. A fluid might be residing in corners or the center. For the fluid in the center, Eqs. (19) and (20) are still used to find the conductance with $A_t$ being the cross-sectional area occupied by that fluid (oil in this case), while conductivity to the fluid residing in the corners is found from Eqs. (B1)–(B6) (see Appendix B).

The conductance to phase $\varrho$ through an assembly of two neighboring elements (pore and throat) connected to each other is considered to be the *harmonic* mean of the conductance to the phase through each element [53]

$$\frac{L_{ij}}{g_{ij}^{\varrho}} = \frac{L_i}{g_i^{\varrho}} + \frac{L_j}{g_j^{\varrho}}, \tag{21}$$

where $L_{ij}$ is the distance between the centers of two connected elements ($R_l$ or $R_w$), $g_{ij}^{\varrho}$ is the conductance of the assembly to phase $\varrho$, $L_i$ and $L_j$ are the half length of the elements $i$ and $j$ ($R_l/2$ or $R_w/2$), and $g_i^{\varrho}$ and $g_j^{\varrho}$ are conductance of the elements $i$ and $j$ to phase $\varrho$, respectively.

The flow rate of phase $\varrho$ between two connected elements, $q_{ij}^{\varrho}$, is then given by [53]

$$q_{ij}^{\varrho} = \frac{g_{ij}^{\varrho}}{L_{ij}}(P_i^{\varrho} - P_j^{\varrho}), \tag{22}$$

where $P_i^{\varrho}$ and $P_j^{\varrho}$ are the pressures of fluid $\varrho$ in elements $i$ and $j$, respectively.

Conserving volume for phase $\varrho$ in each element gives

$$\sum_{i=1}^{m_i} q_{ij}^{\varrho} = 0, \tag{23}$$

where $m_i$ is the number of elements containing continuous phase $\varrho$. If Eq. (21) is written for all such assemblies and then inserted into Eq. (23), a system of linear equations is formed for the pore and throat pressures that is solved using the *conjugate gradient* method [48]. Having the pressures allows us to compute the total flow rate of phase $\varrho$, $Q_{\text{total}}^{\varrho}$, which in turn is used in Eq. (18) to calculate the absolute permeability of the network, $K$. Table III presents the absolute permeability of the networks that were constructed using four coarse fracture aperture maps (see Table II).

Relative permeabilities are computed only when the system contains more than one phase and only for phases that have at least one network-spanning cluster (a cluster that is continuous from inlet to outlet). First conductance in all the elements that contain continuous phase $\varrho$ is computed. Then by utilizing the procedure used for the calculation of absolute permeability, phase pressures in all the pores and throats that belong to the network-spanning cluster(s) are found. The relative permeabilities during capillary dominated drainage and imbibition simulations are calculated from

$$k_r^{\varrho} = \frac{Q_{\text{total}}^{\varrho}}{Q_{\text{total}}^{\text{sp}}} \tag{24}$$

where sp stands for single phase.

For quasidynamic simulations of imbibition, we utilize a method that is similar to the one used by Hughes and Blunt [10]. Displacements are ranked based on their $P_{\text{rank}}$ that is calculated from

$$(P_{\text{rank}})^i = (\Delta P^w)^i - (P_{\text{cow}}^{\text{th}})^i - \Delta\rho g(\Delta l)^i \sin\zeta, \tag{25}$$

where $(P_{\text{rank}})^i$ is the ranking pressure for a displacement of oil by water in element $i$, $(\Delta P^w)^i$ is the water pressure drop between the inlet and element $i$, $(P_{\text{cow}}^{\text{th}})^i$ is the threshold oil-water capillary pressure for invasion of water into oil in element $i$, $\Delta\rho$ is the difference between densities of oil and water, $g$ is the gravitational constant, $(\Delta l)^i$ is the distance from the inlet to the center of element $i$, and $\zeta$ is the angle that the central plane, along the length, of the fracture makes with the horizontal.

To simulate quasidynamic imbibition, first we assume an arbitrary pressure drop across the network and solve for pressure field, which in turn allows us to compute water flow rate. This is done assuming that water flow rate is constant throughout the network. Then, water pressure drop is adjusted accordingly to allow a water flow rate that is similar to the experimentally measured value. The resultant pressure field is used in Eq. (25) to rank the displacements. The pressure field is updated after every 20 displacements. More frequent pressure field updates did not affect the results, presented in part II of this work (see Ref. [30]), significantly.

Relative permeabilities for quasidynamic simulations of imbibition are computed using a pseudo method used by Hughes and Blunt [10]

$$k_r^{\varrho} = \frac{P_{\text{inlet}}^{\text{sp}} - P_{\text{outlet}}^{\text{sp}}}{P_{\text{inlet}}^{\varrho} - P_{\text{outlet}}^{\varrho}}, \tag{26}$$

where $P_{\text{inlet}}^{\text{sp}}$ and $P_{\text{outlet}}^{\text{sp}}$ are inlet and outlet pressures in a single-phase system, while $P_{\text{inlet}}^{\varrho}$ and $P_{\text{outlet}}^{\varrho}$ are inlet and outlet pressures of phase $\varrho$ in a multiphase system.

### A. Model assumptions

In this work, it is assumed that the fluids are Newtonian, incompressible, and immiscible. It is also assumed that primary and secondary drainage processes are capillary dominated ignoring rate and gravity effects. To model imbibition we take into account capillary, rate, and gravity effects ignoring pressure drop in the nonwetting phase (oil). In the execution of the experiments, oil and water phases were thoroughly mixed and presaturated with each other to prevent further mass transfer during core floods. Accordingly, the model neglects mutual solubility of the fluid phases when modeling displacement mechanisms. Temperature is also fixed to prevent changes in solubility of fluids in each other. These two assumptions ensure that interfacial tension stays the same during different processes. In our computations of phase conductance we consider no-flow boundary for all oil-water interfaces as proposed by Zhou *et al.* [47].

In reality layers closer to the inlet are thicker than those that are closer to the outlet. The conductance associated with the thin layers (close to the outlet) can be small enough to prevent us from finding a solution for the pressure field [10]. Therefore, similar to the procedure used by Hughes and Blunt [10] we assign a fixed conductance to the wetting layers when quasidynamic imbibition is simulated. Fluid conductance through the layers is adjusted using parameter $\lambda$, which is defined as

$$\lambda = \frac{\text{average conductivity of fully saturated elements}}{\text{wetting layer conductivity}}. \tag{27}$$

Also flow rate is assumed to be constant throughout the network.

## VI. CONCLUDING REMARKS

We propose a pore-scale network model to study two-phase displacements in a rough-walled fracture. In this study, x-ray imaging techniques proved useful to extract an exact replica of the fracture's inner structure and void volume for the construction of a network model. We were able to characterize the void space and wetting properties of a single fracture with sufficient details to build a robust model to predict fracture transport properties and fluid distributions. We also propose a different method to estimate advancing and receding contact angles using x-ray microtomography

images, and a controlled interface growth model to match oil-water interface curvatures from drainage and imbibition experiments. We present a methodology for modeling two-phase flow in fractures with complex internal geometry, which can be used as a platform for studying immiscible transport phenomena in fractured formations. Results of the implementation of the proposed pore-scale network model are presented in part II of this work; see Ref. [30].

## ACKNOWLEDGMENTS

The Center for Quantitative Imaging at the Pennsylvania State University, and the Enhanced Oil Recovery Institute of the University of Wyoming are gratefully thanked for their support. We also thank R. G. Hughes (Louisiana State University), M. J. Blunt (Imperial College London), and A. S. Grader (The Pennsylvania State University) for the valuable discussions.

## APPENDIX A: SOME USEFUL GEOMETRICAL RELATIONSHIPS

The length of contact line between oil and water at a corner is given by

$$L_{\mathrm{ow,c}} = 2r_{\mathrm{ow}}\left[\frac{\pi}{2} - (\theta_k + \alpha)\right], \tag{A1}$$

where $r_{\mathrm{ow}}$ is the radius of curvature which corresponds to the ratio of interfacial tension to the capillary pressure of the interface, $\alpha$ is the corner half angle, $\pi/4$ for elements with rectangular cross section, and $\theta_k$ is the angle that the interface makes with the solid surface towards the corner which is the contact angle in this work, $\theta_{\mathrm{ow}}$. This could be $\theta^r_{\mathrm{ow}}$, $\theta^h_{\mathrm{ow}}$, or $\theta^a_{\mathrm{ow}}$. The meniscus-apex distance of an interface in a corner is calculated using

$$b = r_{\mathrm{ow}}\frac{\cos(\theta_k + \alpha)}{\sin\alpha}. \tag{A2}$$

The corner area open to flow is given by

$$A_{w,c} = r^2_{\mathrm{ow}}\left\{\frac{\cos(\alpha+\theta_k)}{\sin\alpha}\cos\theta_k - \left[\frac{\pi}{2} - (\theta_k+\alpha)\right]\right\}. \tag{A3}$$

The area open to flow to a phase in the center of an angular element is the total area of the element minus the summation of the corner areas.

If there is a contact angle hysteresis, oil-water contact angle will hinge from the receding value towards the advancing value during imbibition. The intermediate values are called hinging contact angles and are calculated using

$$\theta^h_{\mathrm{ow}} = \cos^{-1}\left[\frac{r^d_{\mathrm{ow}}}{r^{\mathrm{im}}_{\mathrm{ow}}}\cos(\theta^r_{\mathrm{ow}} + \alpha)\right] - \alpha. \tag{A4}$$

Hinging contact angles are used, during imbibition, to calculate $L_{\mathrm{ow}}$ and $A_{w,c}$ only when $\theta^h_{\mathrm{ow}} < \theta^a_{\mathrm{ow}}$.

## APPENDIX B: CONDUCTANCE

Several authors have proposed expressions to compute the conductance of wetting layers [29,49,56–60]. In this work, we use the expressions proposed by Zhou *et al.* [47,49]. When $\theta_{\mathrm{ow}} \le \pi/2 - \alpha$ conductance of the element to the phase flowing at the corner in rectangular capillary tubes is given by

$$g = \frac{4A_{w,c}r^2_{\mathrm{ow}}}{\beta\mu_w}, \tag{B1}$$

$$\beta = \frac{12\sin^2\alpha(1-\Omega)^2(\varphi_1 - \Omega\varphi_2)(\varphi_3 + f\Omega\varphi_2)^2}{(1-\sin\alpha)^2\Omega^2(\varphi_1 - \Omega\varphi_2)^3}, \tag{B2}$$

$$\varphi_1 = \cos\theta(\cos\theta - \sin\theta), \tag{B3}$$

$$\varphi_2 = 1 - \frac{4\theta}{\pi}, \tag{B4}$$

$$\varphi_3 = \cos\theta - \sin\theta, \tag{B5}$$

$$\Omega = \frac{\pi}{4}, \tag{B6}$$

where $\theta = \theta_{\mathrm{ow}}$ and $f = 1$ for a no-flow boundary condition suitable for oil-water interfaces [47,49]. One should note that $\theta_{\mathrm{ow}}$ could be $\theta^r_{\mathrm{ow}}$, $\theta^h_{\mathrm{ow}}$, or $\theta^a_{\mathrm{ow}}$.

[1] I. Fatt, Trans. Am. Inst. Min., Metall. Pet. Eng. **207**, 144 (1956).
[2] I. Fatt, Trans. Am. Inst. Min., Metall. Pet. Eng. **207**, 160 (1956).
[3] I. Fatt, Trans. Am. Inst. Min., Metall. Pet. Eng. **207**, 164 (1956).
[4] B. Berkowitz and R. P. Ewing, Surv. Geophys. **19**, 23 (1998).
[5] M. J. Blunt, Curr. Opin. Colloid Interface Sci. **6**, 197 (2001).
[6] M. J. Blunt, M. D. Jackson, M. Piri, and P. H. Valvatne, Adv. Water Resour. **25**, 1069 (2002).
[7] I. Chatzis and F. A. L. Dullien, J. Colloid Interface Sci. **91**, 199 (1983).
[8] R. Lenormand, in *Physics and Chemistry of Porous Media II*, edited by J. R. Banavar, J. Koplik, and K. W. Winkler (American Institute of Physics, New York, 1987), pp. 98–115.
[9] K. K. Mohanty, H. T. Davis, and L. E. Scriven, Paper SPE 9406, Proceedings of the 55th SPE Annual Technical Conference and Exhibition, Dallas, Texas, September 21–24, 1980.
[10] R. G. Hughes and M. J. Blunt, Adv. Water Resour. **24**, 409 (2001).
[11] R. G. Hughes and M. J. Blunt, Transp. Porous Media **40**, 295 (2000).
[12] R. G. Hughes and M. J. Blunt, SPEJ **6**, 126 (2001).
[13] R. Lenormand, E. Touboul, and C. Zarcone, J. Fluid Mech.

**189**, 165 (1988).
[14] V. H. Nguyen, A. P. Sheppard, M. A. Knackstedt, and W. V. Pinczewski, J. Pet. Sci. Eng. **52**, 54 (2006).
[15] R. J. Glass and L. Yarrington, Geoderma **70**, 231 (1996).
[16] R. J. Glass, M. J. Nicholl, and L. Yarrington, Water Resour. Res. **34**, 3215 (1998).
[17] H. Behbahani and M. J. Blunt, SPEJ **10**, 466 (2005).
[18] M. Gladkikh and S. Bryant, Paper SPE 90333, Proceedings of the SPE Annual Technical Conference and Exhibition, Houston, TX, September 26–29, 2004.
[19] A. A. Keller, M. J. Blunt, and P. V. Roberts, Transp. Porous Media **38**, 189 (2000).
[20] K. Pruess and Y. W. Tsang, Water Resour. Res. **26**, 1915 (1990).
[21] A. Aydin, Environ. Geol. **40**, 672 (2001).
[22] S. P. Bertels, D. A. DiCarlo, and M. J. Blunt, Water Resour. Res. **37**, 649 (2001).
[23] S. R. Brown, A. Caprihan, and R. Hardy, J. Geophys. Res., [Solid Earth] **103**, 5125 (1998).
[24] A. A. Keller, Int. J. Rock Mech. Min. Sci. **34**, 358 (1997).
[25] A. A. Keller, Int. J. Rock Mech. Min. Sci. **35**, 1037 (1998).
[26] L. J. Pyrak-Nolte, C. D. Montemagno, and D. D. Nolte, Geophys. Res. Lett. **24**, 2343 (1997).
[27] M. Piri and M. J. Blunt, Phys. Rev. E **71**, 026301 (2005).
[28] M. Piri and M. J. Blunt, Phys. Rev. E **71**, 026302 (2005).
[29] R. Lenormand and C. Zarcone, Paper SPE 13264, Proceedings of the 59th SPE Annual Technical Conference and Exhibition, Houston, TX, September 16–19, 1984.
[30] M. Piri and Z. T. Karpyn, following paper, Phys. Rev. E **76**, 016316 (2007).
[31] Z. T. Karpyn, A. S. Grader, and P. M. Halleck, J. Colloid Interface Sci. **307**, 181 (2007).
[32] H. J. Vinegar and S. L. Wellington, Rev. Sci. Instrum. **58**, 96 (1987).
[33] R. G. Hughes and M. J. Blunt, Paper SPE 56411, Proceedings of the SPE Annual Technical Conference and Exhibition, Houston, Texas, October 3–6, 1999.
[34] A. W. Adamson and A. P. Gast, *Physical Chemistry of Surfaces*, 6th ed. (John Wiley and Sons, Inc., New York, 1997).
[35] N. R. Morrow, J. Can. Pet. Technol. **14**, 42 (1975).
[36] N. R. Morrow, J. Can. Pet. Technol. **15**, 49 (1976).
[37] G. Mason and N. R. Morrow, J. Colloid Interface Sci. **141**, 262 (1991).
[38] R. P. Mayer and R. A. Stowe, J. Colloid Sci. **20**, 893 (1965).
[39] H. M. Princen, J. Colloid Interface Sci. **30**, 69 (1969).
[40] H. M. Princen, J. Colloid Interface Sci. **30**, 359 (1969).
[41] H. M. Princen, J. Colloid Interface Sci. **34**, 171 (1970).
[42] M. Piri and M. J. Blunt, Phys. Rev. E **70**, 061603 (2004).
[43] A. Firoozabadi, *Thermodynamics of Hydrocarbon Reservoirs* (McGraw-Hill, New York, 1999).
[44] R. Lenormand, C. Zarcone, and A. Sarr, J. Fluid Mech. **135**, 337 (1983).
[45] T. C. Ransohoff and C. J. Radke, J. Colloid Interface Sci. **121**, 392 (1988).
[46] S. Bakke and P. E. Øren, SPEJ **2**, 136 (1997).
[47] D. Zhou, M. J. Blunt, and F. M. Orr, J. Colloid Interface Sci. **187**, 11 (1997).
[48] P. E. Øren, S. Bakke, and O. J. Arntzen, SPEJ **3**, 324 (1998).
[49] M. H. Hui and M. J. Blunt, J. Phys. Chem. B **104**, 3833 (2000).
[50] T. W. Patzek, SPEJ **6**, 144 (2001).
[51] P. E. Øren and S. Bakke, Transp. Porous Media **46**, 311 (2002).
[52] M. J. Blunt, J. Pet. Sci. Eng. **20**, 117 (1998).
[53] D. H. Fenwick and M. J. Blunt, Adv. Water Resour. **21**, 121 (1998).
[54] S. Bryant and M. J. Blunt, Phys. Rev. A **46**, 2004 (1992).
[55] T. W. Patzek and D. B. Silin, J. Colloid Interface Sci. **236**, 295 (2001).
[56] M. J. Blunt, D. Zhou, and D. H. Fenwick, Transp. Porous Media **20**, 77 (1995).
[57] P. A. Goode and T. S. Ramakrishnan, AIChE J. **39**, 1124 (1993).
[58] T. C. Ransohoff, P. A. Gauglitz, and C. J. Radke, AIChE J. **33**, 753 (1987).
[59] T. W. Patzek and J. G. Kristensen, J. Colloid Interface Sci. **236**, 305 (2001).
[60] A. Al-Futaisi and T. W. Patzek, SPEJ **8**, 252 (2003).